JACS
JOURNAL OF THE AMERICAN CHEMICAL SOCIETY
pubs.acs.org/JACS
Article

Short-Chain Acids Sustain InAs Colloidal Quantum Dot Growth during Synthesis, Extending Spectral Response into the Deep Short-Wave Infrared

Hyeong Woo Ban,[▽] Xubiao Li,[▽] Stefan Zeiske, Julian A. Steele, Rafael Eduardo López-Arteaga, Haijiao Lu, Yalong Zou, Moon Gyu Han, Tae-Gon Kim, Cheng Liu, Bin Chen, and Edward H. Sargent*

Cite This: https://doi.org/10.1021/jacs.6c03275

ABSTRACT: III−V colloidal quantum dots (CQDs) with large and well-controlled diameters are of interest in applications from red light emitters to deep short-wave infrared (SWIR) photodetectors, yet nanocluster-seeded syntheses often encounter an empirical "size wall" in the ∼5−8 nm diameter range. Here, we identify monomer release and transfer from nanoclusters to growing seeds as a key kinetic constraint during extended injection and growth. We show that short-chain carboxylic acids (SCCAs) can act as transient ligands that increase nanocluster lability and enhance monomer transfer, enabling continuous growth beyond this plateau. ^{1}H NMR using ^{13}C-labeled acetic acid quantifies a ∼1:1 myristate/acetate ligand ratio on the initial nanoclusters, with diffusion-ordered spectroscopy (DOSY) supporting the transient surface association of acetate; ^{2}H NMR of CQDs grown with deuterated acetic acid (CD_3COOH) shows no residual deuterium signal, indicating that acetate promotes growth without persisting on the final CQD surface. Across a C1 (formic) to C4 (butyric) SCCA screen, C2 (acetic) acid provides the best balance of volatility and lability. Incorporating SCCAs at the nanocluster stage yields InAs CQDs with excitonic features extending up to 1800 nm. XPS and indium K-edge XANES/EXAFS analyses indicate diminished oxide-related features in acetic acid-derived samples compared with size-matched controls. We fabricate photodetectors with a 1520 nm exciton, extending InAs CQD photodetection into the deep SWIR.

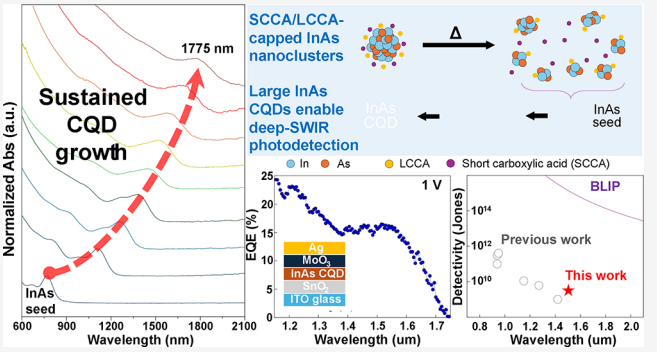

INTRODUCTION

Achieving infrared photodetection at wavelengths beyond 1550 nm is relevant to autonomous sensing,[1−3] biomedical imaging,[4] and environmental monitoring.[5] Traditionally, infrared photodetector devices operating in the short-wave infrared (SWIR, 1000−3000 nm) have relied on epitaxially grown semiconductors such as InGaAs. Despite their success, these materials are constrained in their wider application by the requirement of lattice mismatch and thus the need for substrate compatibility, factors that increase thermal processing requirements and final fabrication costs. Consequently, solution-processed materials compatible with silicon complementary metal-oxide-semiconductor (CMOS) platforms have therefore attracted significant interest.[6−8]

Colloidal quantum dots (CQDs) offer absorption in SWIR,[9] but many of the highest-performing in this band, such as PbS[10−12] and HgTe,[13,14] are subject to the Restriction of Hazardous Substances (RoHS) directive. III−V semiconductor quantum dots, particularly indium arsenide (InAs), are thus receiving added focus.[15,16] To date, size-uniform InAs CQDs have mainly been confined to the near-infrared (NIR), with the $1S^{e}-S^{h}$ transition, i.e., first excitonic peak, not extending beyond 1550 nm.[17−22]

Continuous injection of preformed InAs nanoclusters into InAs seeds is the most widely employed method of synthesis.[23−26] Due to its reliance on continuous injection, this synthetic approach progressively increases the total solution volume and dilutes the reactive species released from nanocluster dissociation, thereby reducing the concentration of growth-active precursors available for sustained particle growth. In addition, carboxylic acids, such as oleic acids, which serve as organic surface capping ligands, undergo a ketonization reaction at elevated temperatures, generating water that leads to surface oxidation and passivates active sites, an additional factor that works against growth. This issue is

Received: February 11, 2026
Revised: April 22, 2026
Accepted: April 28, 2026

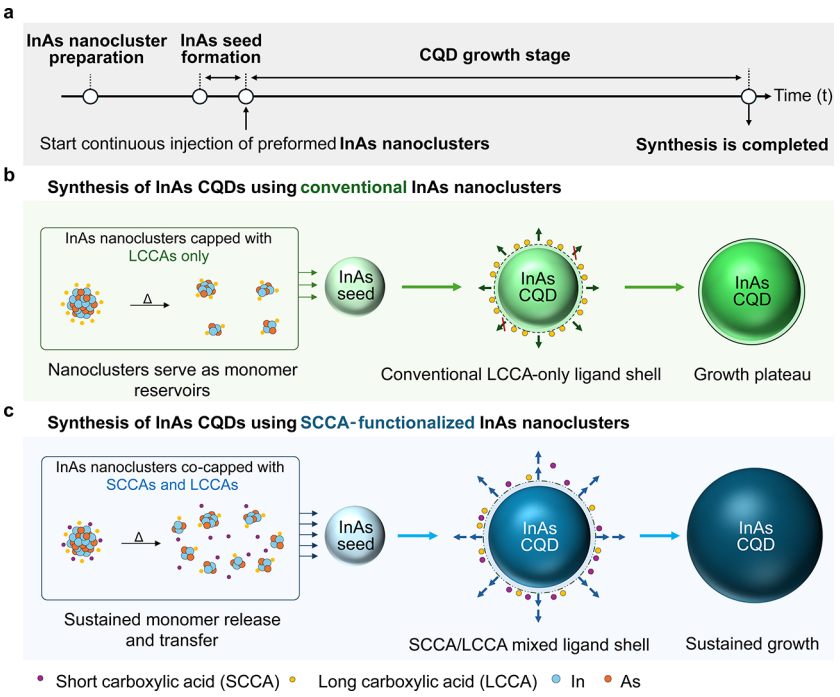

Figure 1. Growth of InAs CQDs from conventional versus SCCA-functionalized nanoclusters. (a) Stages of InAs CQD synthesis involving continuous injection of preformed InAs nanoclusters into an InAs seed solution, highlighting nanocluster preparation, seed formation, and subsequent CQD growth. (b) Under conventional conditions, InAs nanoclusters capped with LCCAs supply monomers to growing seeds, yet growth often reaches a plateau ("size wall") as monomer release and transfer and surface access become increasingly constrained during prolonged injection and growth. (c) In contrast, SCCA-functionalized nanoclusters (cocapped with SCCAs and LCCAs) are proposed to act as more labile monomer reservoirs, enabling sustained monomer release and transfer to the growing seeds and thereby supporting continued growth toward substantially larger CQDs.

expected to be of particular importance in the case of long-chain carboxylic acids (LCCAs) since these serve as the primary organic surface capping ligands, are strongly bound to the InAs nanocluster and growing InAs CQD surface and are therefore more likely to participate in surface-localized reactions. Thus, extending InAs CQDs into the >1500 nm excitonic regime becomes considerably more challenging;[26−28] compared with ensembles in the 950−1100 nm range,[20,29] the band-edge absorption in this long-wavelength regime is often less prominent and less well-resolved, frequently appearing broader or shoulder-like. These considerations motivate the development strategies that sustain monomer release and transfer over the course of extended-duration growth. While both long- and short-chain carboxylic acids can undergo ketonization at elevated temperatures, LCCAs are the dominant and more strongly bound surface ligands and therefore have a greater influence on surface chemistry during growth. In this work, we examine whether SCCAs can function primarily as transient ligands that increase nanocluster lability and facilitate monomer delivery to growing seeds. We find that this strategy sustains InAs CQD growth beyond the apparent size wall and that the resulting CQDs can be used to fabricate SWIR photodetectors with excitonic response extended to 1520 nm.

RESULTS AND DISCUSSION

Diffusion-Limited Growth of InAs CQDs with Conventional Nanoclusters

We studied first the origins of growth limitations in the established nanocluster-based InAs CQD synthesis (Figure 1a). Preformed InAs nanoclusters, typically capped with oleate, are injected into an InAs seed solution, and this is followed by thermal growth. While oleate ligands offer colloidal stability, their sluggish exchange kinetics can contribute to limiting growth.[30] We employed shorter ligand chains to increase precursor access to the InAs seed surface and facilitate monomer supply from the nanoclusters.[31] We found, though, that monomer delivery remained constrained: even with C_{14}-chain LCCAs, monomer release from nanoclusters to the seed surface was insufficient to sustain growth (Supplementary Figure S1). Prolonged injection (e.g., 20 h) failed to shift the first excitonic feature beyond ∼1400 nm. The continuous-injection mode diluted reactive intermediates and lowered supersaturation, preventing sustained growth even when we adjusted nanocluster concentration and injection rate (Supplementary Figure S2−S4). During extended injection and growth, monomer release and transfer and access to the growing seed surface can become increasingly constrained, giving rise to an apparent growth plateau (Figure 1b). In addition, we cannot exclude that oxide formation on the dot surface under the growth conditions may be one of several factors that suppress further size evolution.[32,33] We therefore hypothesized that a relatively unexplored degree of freedom—the reactivity of InAs nanoclusters—could be exploited to increase monomer release during CQD growth. We looked for molecules that could implement two functions: (1) they would act as transient surface ligands, molecules whose more labile and dynamic surface association would render nanoclusters more reactive and thereby facilitate monomer release to the growing seeds; (2) they would reduce the kinetic constraints imposed by long-chain ligand shells at the nanocluster and

https://doi.org/10.1021/jacs.6c03275
J. Am. Chem. Soc. XXXX, XXX, XXX−XXX

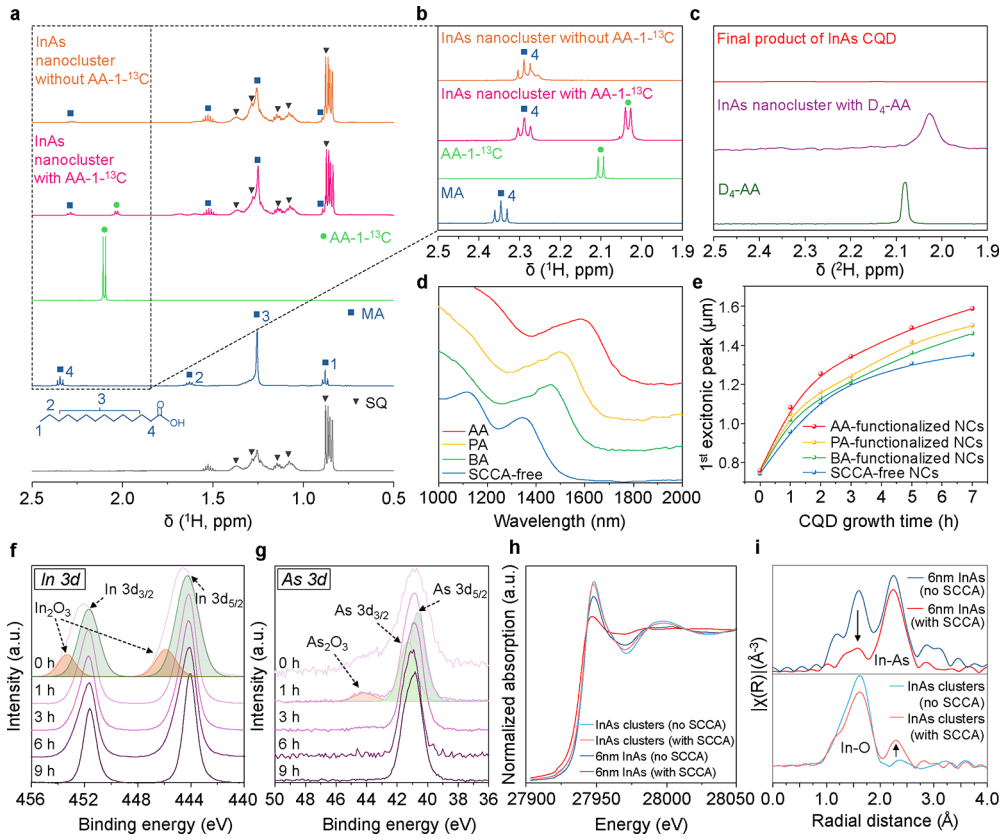

Figure 2. Surface ligand environment and oxide-associated features in short-chain carboxylic acid (SCCA)-treated InAs nanoclusters and CQDs. (a) ^{1}H NMR spectra of squalene (SQ, ▼), myristic acid (MA, ■), ^{13}C-labeled acetic acid (AA-1-^{13}C, ●), and InAs nanoclusters synthesized with and without AA-1-^{13}C. The chemical structure of MA is annotated with the corresponding proton position. Methyl resonances from AA-1-^{13}C appear as a doublet due to ^{1}H−^{13}C coupling, enabling clear assignment in the InAs nanocluster spectra. (b) A magnified view of the spectral region between 2.5 and 1.9 ppm highlights distinct chemical shifts and coupling features for MA and AA-1-^{13}C in the nanocluster environment. (c) ^{2}H NMR spectra of the final product of InAs CQDs (top), InAs nanoclusters with deuterated acetic acid (D_4-AA) (middle), and pure D_4-AA (bottom) to trace surface ligand incorporation. (d) Absorption spectra of InAs CQDs grown from InAs nanoclusters functionalized with different SCCAs. Molecular structures of acetic acid (AA), propionic acid (PA), butyric acid (BA), and myristic acid (MA, SCCA-free control), illustrating variation in alkyl chain length. (e) First excitonic peak positions plotted as a function of reaction time for each condition. Time-resolved X-ray photoelectron spectroscopy (XPS) spectra of (f) In 3d and (g) As 3d core levels in InAs CQDs grown via continuous injection of AA-mediated nanoclusters. (h) In K-edge X-ray absorption near-edge structure (XANES) spectra of InAs nanoclusters and CQDs synthesized with and without SCCA functionalization, showing reduced white-line intensity by SCCAs. (i) Fourier-transformed extended X-ray absorption fine structure (EXAFS) spectra (k^3-weighted) displaying the radial distribution of atomic coordination around indium. The In−O coordination peak (∼1.5 Å) diminishes with CQD growth, while the In−As peak (∼2.4 Å) becomes more pronounced, consistent with reduced white-line intensity in XANES (panel (h)), oxide suppression, and enhanced InAs lattice ordering.

seed interface, enabling continued monomer transfer and attachment.

Short-Chain Carboxylic Acids (SCCAs) as Transient Ligands Modulating InAs CQD Growth

We explored the use of short-chain carboxylic acids (SCCAs) (Figure 1c) with the dual objectives described above. We expected reactivity to arise from dynamic ligand exchange, whereby SCCAs transiently coordinate to surface indium sites, thereby increasing nanocluster lability, facilitating monomer release and delivery to growing seeds. Moreover, the packing of long-chain carboxylate ligands can impose kinetic barriers to surface access and monomer attachment.[34] We therefore hypothesized that introducing SCCAs may perturb long-chain packing and lower these ligand-shell-imposed barriers at the nanocluster/seed interface. Together with their shorter surface residence time and higher volatility, this transient coordination makes SCCAs less prone to persistent surface accumulation, which can help sustain precursor release under the synthesis conditions used here. We began by adding acetic acid (AA) to the nanoclusters. To facilitate ^{1}H nuclear magnetic resonance (NMR) signal assignment (Figure 2a and 2b), we employed ^{13}C-labeled acetic acid (AA-1-^{13}C). Two distinct methyl resonances are observed for surface-bound myristate and acetate ligands, each showing a ∼0.06 ppm downfield shift relative to corresponding free acid references. In ^{13}C-acetic acid, hydrogen bonding from the carboxyl proton perturbs electron density at the carbonyl group, leading to modest deshielding and a downfield shift; whereas acetate anions exhibit enhanced delocalization and greater local shielding, resulting in an upfield shift. These observations underscore the sensitivity of chemical shifts to ligand coordination dynamics. They indicate the coexistence of distinct ligand species on the surface of InAs nanoclusters. Integration of the methyl signals reveals a ∼1:1 molar ratio between myristate and acetate ligands (Supplementary Figure S5). Furthermore, the acetate species are predominantly associated with the nanoclusters, consistent with surface-bound ligands, although a minor

https://doi.org/10.1021/jacs.6c03275
J. Am. Chem. Soc. XXXX, XXX, XXX−XXX

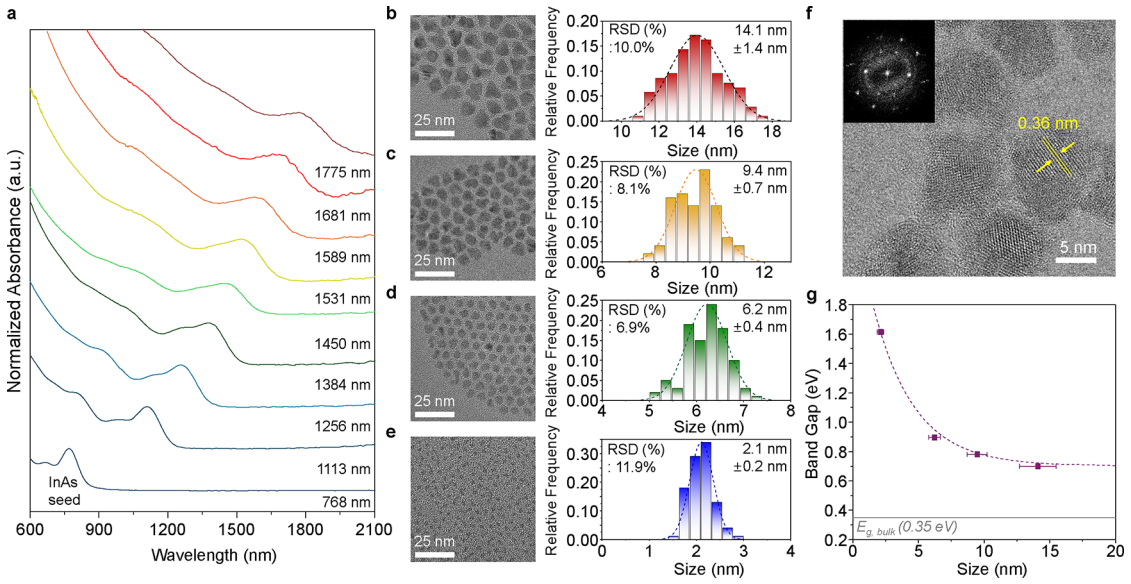

Figure 3. Size-tuned growth of InAs CQDs via continuous injection of SCCA-functionalized InAs nanoclusters. (a) Normalized absorption spectra of InAs CQDs exhibiting first excitonic peaks tunable from 768 to 1775 nm. Transmission electron microscopy (TEM) images and corresponding size distribution histograms of representative CQDs with excitonic peaks at (b) 1775, (c) 1589, (d) 1384, and (e) 768 nm, respectively. Histograms were plotted using an identical bin width across panels; dispersions are reported as relative standard deviation (RSD, %) = (SD/mean) × 100% calculated from N = 100 particles. (f) High-resolution TEM (HRTEM) image of a representative large InAs CQD showing clear lattice fringes with an interplanar spacing of 0.36 nm, consistent with the (111) planes of zinc blende InAs. Inset: Fast Fourier transform (FFT) pattern, confirming the crystalline order of the particle. (g) The sizing curve of InAs CQDs plotted as the energy of the first excitonic peak versus mean particle diameter extracted from TEM images.

fraction of free acetate cannot be entirely excluded (Supplementary Figure S6).

To determine whether acetate ligands remain bound during nanocluster growth, we carried out thermogravimetric analysis (TGA), from which we found that AA-treated nanoclusters decompose at a lower temperature and with greater mass loss than the myristic acid (MA)-only controls (Supplementary Figure S7). This is consistent with higher volatility and less persistent surface association in the case of AA. After nanocluster purification process, however, the AA-treated nanoclusters show lower mass loss compared to the MA-only controls. This suggests that most of the AA is easily removed during purification, further confirming its weak and labile binding to the nanocluster surface. Transient absorption (TA) measurements showed shortened carrier lifetimes in AA-treated nanoclusters (Supplementary Figure S8), suggesting elevated trap densities and incomplete surface passivation. ^{2}H NMR analysis of InAs CQDs synthesized using deuterated acetic acid (CD_3COOH) showed no residual deuterium signal (Figure 2c), i.e., acetic acid does not persist on the CQD surface following growth. From diffusion-ordered spectroscopy (DOSY), MA exhibits lower diffusion coefficients, consistent with tighter surface retention, whereas acetic acid diffuses more rapidly, indicating more labile and less persistent surface association (Supplementary Figure S9). Based on these studies, we propose that acetic acid transiently associates with nascent InAs nanoclusters, promoting monomer conversion efficiency during early growth, but does not persist on the CQD surface following the completion of growth.

We next explored how the chain length of the SCCA influences InAs nanocluster formation. A series of analogues, including acetic, propionic, and butyric acids, was used to synthesize InAs nanoclusters (Supplementary Figure S10). Absorption spectra indicated that nanocluster size increased with alkyl chain length, and all SCCA-treated samples showed larger sizes than that of the SCCA-free control. SCCAs thus promote the reactivity of indium and arsenic precursors, facilitating growth. When injected into InAs seed solutions, SCCA-treated nanoclusters yielded CQDs with red-shifted first excitonic peaks relative to the control (Figure 2d), i.e., these led to increased CQD size. Time-resolved absorption measurements tracked the excitonic peak position over reaction time (Figure 2e), showing the same SCCA-accelerated growth kinetics. Of the SCCAs evaluated, acetic acid (C2) demonstrated the highest growth acceleration (Supplementary Figure S11). We suggest that the slower growth in the case of formic acid (C1)-treated nanoclusters relates to its higher volatility. By contrast, we interpret the reduced effectiveness of the C3 and C4 analogues relative to C2 as reflecting a less favorable balance between transient ligand behavior and alkyl-chain length, as increasing chain length is expected to reduce their ability to relieve ligand-shell-imposed kinetic barriers during monomer release and transfer.

We focused our subsequent studies on acetic acid (Figure 3) and examined how SCCA functionalization correlates with oxidation-associated features across the size series. InAs CQDs synthesized with LCCAs often exhibit surface oxide components such as In_2O_3 and As_2O_3, which can limit further growth and degrade optoelectronic properties.[24] X-ray photoelectron spectroscopy (XPS) shows that the use of AA-treated nanoclusters correlates with a progressive reduction in surface oxide features during growth (Figure 2f and 2g). Indium K-edge X-ray absorption near-edge spectroscopy (XANES), using size-matched dot comparisons (Figure 2h), also reveals a weaker white-line intensity when AA is employed, suggesting reduced oxide-like character already at the nanocluster stage. This characteristic is evident in nanoclusters and ~9 nm InAs CQDs, but diminishes in ~14 nm InAs CQDs, where the

https://doi.org/10.1021/jacs.6c03275
J. Am. Chem. Soc. XXXX, XXX, XXX−XXX

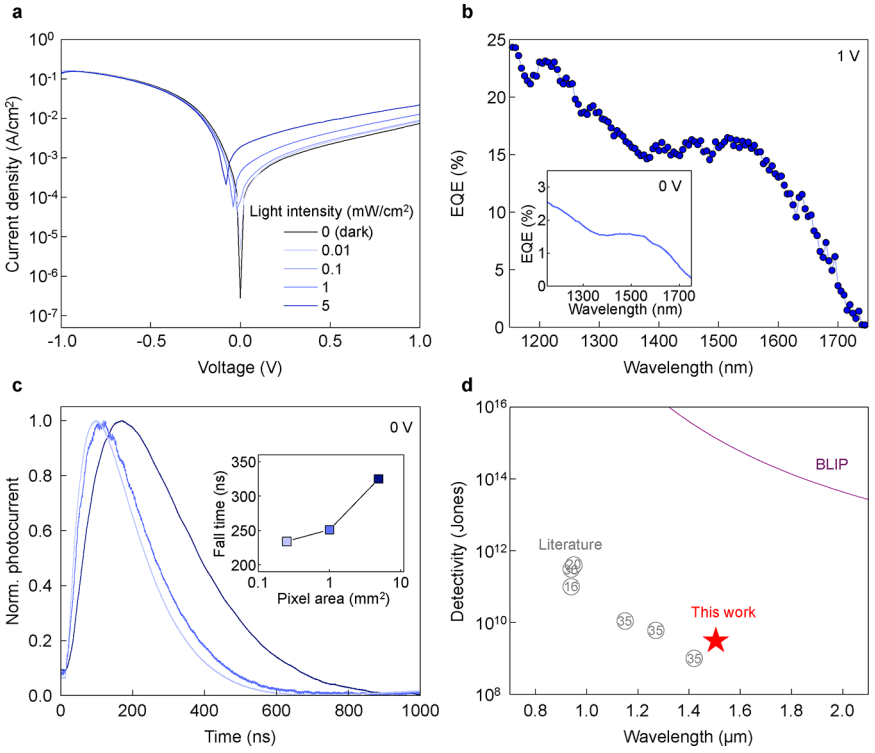

Figure 4. Optoelectronic performance of SWIR InAs CQD photodiodes. (a) Current density versus voltage (J−V) characteristics measured in the dark and under 1310 nm illumination at various power densities. (b) Wavelength-dependent EQE at 1 V forward bias. The inset shows the corresponding EQE obtained under zero bias voltage. (c) Normalized photocurrent transient for varying circular pixel areas (0.25, 1, and 4.9 mm^2), with active areas defined by the geometric overlap of the ITO bottom electrode and the circular Ag top electrode deposited via a shadow mask, measured under illumination restricted to each pixel using a matching aperture, as obtained under short-circuit conditions. (d) Calculated detectivity for the SWIR InAs CQD photodiode studied in this work (star) and narrow-gap InAs CQD-based photodetectors from the literature (circles).[16,20,35,36] The purple solid line corresponds to the theoretical background-limited photodetector limit (BLIP) at 300 K.

white-line intensity approaches that of bulk InAs, consistent with a more bulk-like local coordination environment and reduced oxide-like contributions (Supplementary Figure S12a). Extended X-ray absorption fine structure (EXAFS; Figure 2i) shows that the In−O coordination feature at ∼1.5 Å, prominent in nanoclusters, diminishes as particle size increases, while the In−As feature at ∼2.4 Å becomes more defined, particularly for the 14 nm InAs CQDs (Supplementary Figure S12b and S13). This evolution is consistent with a decreasing In−O contribution and an increasingly In−As-dominated local environment with increasing particle size. Quantitative analysis of the In−O to In−As coordination ratio (Supplementary Figure S12c) likewise shows that InAs nanoclusters synthesized without AA exhibit an In−O/In−As ratio that is ∼8× higher than that of AA-treated counterparts. Consistent trends emerge from size-matched comparisons: oxidation-associated features become more pronounced at smaller diameters (higher surface-to-volume ratio), whereas AA-derived samples exhibit weaker oxide-related contributions even at comparable sizes (Supplementary Figure S12d). Taken together, these observations support AA as a transient ligand that sustains growth beyond the apparent size wall, with reduced oxide-associated contributions observed across the resulting InAs CQD size series.

Synthesis of Larger-Sized InAs CQDs

We therefore turned to exploring (Figure 3a) whether SCCAs could enable extended growth and large InAs CQDs. Excitonic features are well-defined for dot sizes selected across the SWIR region (750−1800 nm), results achieved without postsynthetic size-selective precipitation. X-ray diffraction (XRD) reveals a narrowing of the full width at half-maximum (fwhm) for the (111), (220), and (311) peaks (Supplementary Figure S14), consistent with the increase in crystallite domain sizes. Transmission electron microscopy (TEM) images directly visualize the progressive increase in CQD diameter, consistent with the expected size evolution, while the corresponding size histograms quantify the diameter dispersion (Figure 3b−3e). In the ≥ 8 nm size regime, the ensembles maintain RSD values in the ∼8−10% range, indicating good size uniformity. HRTEM further confirms the crystallinity of the larger InAs CQDs, showing clear lattice fringes with a spacing of 0.36 nm assignable to the (111) planes of zinc blende InAs (Figure 3f). In addition, the sizing curve reveals the expected correlation between first excitonic transition energy and mean particle diameter, consistent with controlled size evolution across the full series (Figure 3g). To our knowledge, this represents the first report of InAs CQDs exhibiting excitonic features at ∼1800 nm.

We found that an AA:In precursor molar ratio of 3:1 is optimal for sustaining InAs CQD growth while preserving size uniformity. Figure 3a shows the corresponding growth trajectory; additional AA loadings (1.5:1 and 4.5:1) are compared in Supplementary Figure S15. Higher AA loading (4.5:1) accelerates CQD growth but also broadens the excitonic line width. We note that precursor volatility and side reactions at elevated AA concentrations may disrupt the controlled growth of CQDs. We investigated whether introducing AA during seed synthesis could enhance

https://doi.org/10.1021/jacs.6c03275
J. Am. Chem. Soc. XXXX, XXX, XXX−XXX

subsequent CQD growth: it had no measurable effect on seed size, yet subsequent AA accumulation during the injection of AA-functionalized nanoclusters led to overgrowth and polydispersity (Supplementary Figure S16). In summary, moderate AA levels facilitate controlled growth, whereas an excess disrupts dot monodispersity, and total SCCA content must be managed throughout the reaction.

InAs CQD-Based SWIR Photodetectors

Space-charge-limited current (SCLC) measurements were performed to estimate the trap-state density of 1520 nm InAs CQD films in the oxide-free and surface-oxidized states (Supplementary Figure S17). The oxide-free CQD films exhibit a significantly reduced trap density, indicating improved electronic quality that is beneficial for device performance. Based on this, we used 1520 nm-sized InAs CQDs capped with inorganic halides ($InBr_3$) to fabricate photodetectors (Supplementary Figure S18 and the Experimental Section). As shown in Figure 4a, the dark current density is 3×10^{-7} A/cm^2 at short circuit and 7×10^{-3} A/cm^2 under an applied bias of 1 V. When we illuminate at 5 mW/cm^2 and apply 1 V of bias, the photocurrent reaches 2×10^{-2} A/cm^2, corresponding to an external quantum efficiency (EQE) of 16% at 1520 nm. Power-dependent photocurrent measurements showed sublinear behavior over the measured range, with the most nearly linear response observed between 0.1 and 1 mW/cm^2 ($\alpha \approx 0.73$), indicating that the reported EQE is not associated with a superlinear gain response (Supplementary Figure S19). We note the need to further improve devices and contacts in the future to reach higher unbiased EQE (inset, Figure 4b). When we optimized pixel sizes, we achieved transient photocurrent (TPC) responses $\tau \approx$ 240 ns. The area dependence of the transients in Figure 4c indicates a strong correlation with device RC effects, with smaller pixels showing faster response consistent with reduced capacitance. The present value should therefore be interpreted as the device-level response time of the current architecture, rather than as the intrinsic hopping-transport limit of the InAs CQD layer.

We obtained detectivity (D*) according to $D^* = R\sqrt{(A\Delta f)}/i_n$, where R is the responsivity, A is the pixel area (cm^2), Δf is the electrical bandwidth (Hz), and i_n is the experimentally measured noise current. Using $\Delta f = 1$ Hz, we obtained $D^* = 1 \times 10^9$ Jones at 1520 nm under a 1 V bias. For comparison, the purple solid line in Figure 4d indicates the background-limited infrared photodetector (BLIP) limit at 300 K, which represents the theoretical performance ceiling for an ideal radiative photodiode whose noise is set solely by background photon flux.

To contextualize this performance, we compared it with previously reported InAs CQD-based photodetectors operating in the 0.9−1.5 μm range (Figure 4d and Supplementary Table S1).[16,20,35,36] Prior studies on InAs-based CQD NIR photodetectors have achieved detectivities of 10^{12} Jones at 950 nm,[20,36] but their EQE was not extensible beyond 1400 nm. The present work thus contributes a value at 1520 nm.

CONCLUSION

The pronounced CQD growth enhancement observed herein can be rationalized by the distinct roles of the dual-ligand system in InAs nanoclusters. LCCAs provide strong surface passivation and colloidal stability, yet their bulky, tightly bound nature can hinder monomer access to reactive surface sites. In contrast, SCCAs, which are smaller and thermally labile, desorb more readily under synthesis conditions, transiently exposing reactive In and As species. This promotes monomer incorporation into the growing seed lattice. Meanwhile, the remaining LCCAs sustain colloidal stability and suppress uncontrolled aggregation. Cocapping with SCCAs and LCCAs thus enables sustained yet controlled CQD growth, extending the accessible InAs CQD size range and shifting the excitonic transition to longer SWIR wavelengths.

The resulting InAs CQDs enable a 1520 nm photodetector with a peak EQE of ∼16% and a detectivity of $\sim 1.4 \times 10^9$ Jones, extending InAs CQD photodetectors into the deep-SWIR. More broadly, reactivity control over nanoclusters as synthetic intermediates introduces a tunable degree of freedom that can be leveraged to overcome growth plateaus while maintaining surface passivation in CQD synthesis.

EXPERIMENTAL SECTION

Materials

Myristic acid (MA) (98%, Sigma-Aldrich), stearic acid (SA) (97%, Sigma-Aldrich), oleic acid (OA) (technical grade (90%), Sigma-Aldrich), formic acid (FA) (98%−100%, Sigma-Aldrich), acetic acid (AA) (99.99%, Sigma-Aldrich), acetic acid-d4 (AA-d4) (≥99.5 atom %, Sigma-Aldrich), acetic acid-1-^{13}C (AA-1-^{13}C) (99 atom % ^{13}C, Sigma-Aldrich), propionic acid (PA) (≥99.5%, Sigma-Aldrich), butyric acid (BA) (≥99.5%, Sigma-Aldrich), Indium(III) acetate ($In(OAc)_3$) (99.99%, Sigma-Aldrich), tris(trimethylsilyl)arsine ($(TMSi)_3As$) (Sigma-Aldrich), dioctylamine (DOA) (97%, Sigma-Aldrich), squalane (SQ) (technical grade (≥90%), Sigma-Aldrich), hexane (anhydrous, 95%, Sigma-Aldrich), 1-butanol (BuOH) (anhydrous 99.8%, Sigma-Aldrich), toluene (anhydrous, 99.8%, Sigma-Aldrich), *N*,*N*-dimethylformamide (DMF) (anhydrous 99.8%, Sigma-Aldrich), indium(III) bromide (99.999%, Sigma-Aldrich), and ammonium acetate (99.999%, Sigma-Aldrich) were used in the experiments. All reagents and chemicals were used as received without further purification.

Synthesis of InAs Colloidal Quantum Dots (CQDs)

The synthesis of InAs CQDs is based on the continuous hot injection method, where the presynthesized InAs nanoclusters were gradually injected into the synthesized InAs seeds at elevated temperatures. All procedures were conducted inside nitrogen-filled gloveboxes to prevent oxidation and minimize the leakage of toxic arsenic precursors. Additionally, the squalene as a noncoordinating solvent was degassed at 110 °C overnight prior to use.

Synthesis of InAs Nanocluster without Short Carboxylic Acids. The indium precursor solution was prepared by dissolving $In(OAc)_3$ (8 mmol, 2.335 g) and MA (24 mmol, 5.481 g) in degassed SQ (20 mL) in a 250 mL round-bottom flask. The mixture was degassed at 120 °C overnight to form $In(MA)_3$. Following degassing, the flask was refilled with nitrogen gas and maintained at 65 °C. For the arsenic precursor, $(TMSi)_3As$ (4 mmol, 1.185 mL) was dissolved in a mixture of DOA (16 mmol, 4.845 mL) and degassed SQ (8 mL). The solution was stirred at 60 °C for 20 min to ensure homogeneity. The arsenic precursor solution was then injected into the flask containing the indium precursor solution at 65 °C and stirred for an additional 20 min to synthesize InAs nanoclusters.

Synthesis of InAs Nanocluster with Short Carboxylic Acids. The indium precursor solution was prepared by dissolving $In(OAc)_3$ (8 mmol, 2.335 g) and MA (24 mmol, 5.481 g) in degassed SQ (20 mL) in a 250 mL round-bottom flask. The mixture was degassed at 120 °C overnight. After degassing, the flask was refilled with nitrogen gas and maintained at 65 °C. For the arsenic precursor, $(TMSi)_3As$ (4 mmol, 1.185 mL) was dissolved in a mixture of DOA (16 mmol, 4.845 mL) and degassed SQ (8 mL). The solution was stirred at 60 °C for 20 min. Subsequently, 24 mmol of a carboxylic acid having a short carbon chain length, such as FA (0.905 mL), AA (1.374 mL),

https://doi.org/10.1021/jacs.6c03275
J. Am. Chem. Soc. XXXX, XXX, XXX−XXX

PA (1.790 mL), or BA (2.203 mL), was added to the indium precursor solution at 65 °C and stirred for 5 min to ensure thorough mixing. Finally, the arsenic precursor solution was injected into the indium precursor solution at 65 °C and stirred for an additional 20 min.

Synthesis of InAs Seeds. The indium precursor solution for InAs seed was prepared in a separate flask by dissolving $In(OAc)_3$ (1 mmol, 0.292 g) and MA (3 mmol, 0.685 g) in degassed SQ (5 mL). The mixture was then degassed at 120 °C overnight. Then the flask was refilled with nitrogen gas and heated up to 320 °C. For the preparation of the arsenic precursor solution, $(TMSi)_3As$ (0.5 mmol, 0.148 mL) was dissolved into the mixture of DOA (2 mmol, 0.604 mL) and degassed SQ (1 mL), and the solution was stirred at 60 °C for 20 min. The prepared arsenic precursor solution was then quickly injected into the indium precursor solution at 320 °C and stirred for 5 min to make InAs seeds.

Synthesis of InAs CQDs. The presynthesized InAs nanocluster solution, with or without short-chain ligands, was transferred into a 20 mm-diameter syringe connected to a syringe pump. Upon completion of the InAs seed growth, the syringe pump gradually delivered the InAs nanocluster solution into the flask containing the InAs seed solution at a fixed injection rate of 3 mL/h while maintaining a temperature of 312 °C. Once the desired InAs CQDs size was achieved, the reaction was quenched by rapidly cooling the flask to room temperature. It is recommended to add a sufficient amount of nonpolar solvents before the temperature of the reaction flask drops below 60 °C to prevent the solidification of InAs CQDs capped with MA, as the melting point of MA is 54.4 °C. For purification, the crude InAs CQD solution was first centrifuged at 7800 rpm for 5 min. The supernatant was collected and filtered through a 2 μm filter. Anhydrous BuOH was then added to the filtered supernatant at a 1:1 volume ratio (v/v), followed by centrifugation at 7800 rpm for 5 min to remove larger particles or byproducts as precipitates. The resulting supernatant was precipitated again by adding additional anhydrous BuOH at a 2:1 v/v ratio and centrifuged again under the same conditions. The final precipitate was dispersed in anhydrous *n*-hexane. To further purify the InAs CQDs, this purification process was repeated two times more. Finally, the purified InAs CQDs were dispersed in anhydrous *n*-hexane and stored in a N_2-filled glovebox for subsequent experiments.

Ligand Exchange Process

The ligand exchange process for InAs CQDs was conducted inside a nitrogen-filled glovebox, following previously reported methods with slight modifications. Initially, 0.36 g of indium(III) bromide and 0.046 g of ammonium acetate were dissolved in 10 mL of DMF under stirring. The resulting exchange solution was then filtered using a 0.22 μm filter. Subsequently, 1 mL of InAs CQD solution (50 mg mL^{-1} in anhydrous *n*-hexane) was introduced into a plastic tube containing 10 mL of exchange solution and 15 mL of *n*-hexane. The mixture was vigorously vortexed until the CQDs were transferred completely from the upper hexane phase to the bottom DMF phase. The upper hexane layer was discarded and replaced with fresh hexane, a step that was repeated twice. To isolate the CQDs from DMF, anhydrous toluene (DMF:toluene = 1:1.5 v/v) was added, and the solution was centrifuged for 5 min. Finally, the precipitated CQDs were redispersed in DMF at a high concentration of 300 mg mL^{-1}.

Device Fabrication

The 2.5 cm × 2.5 cm glass substrate, patterned with ITO, was cleaned by sonication in DI water, acetone, and isopropanol for 30 min each, and then fully dried by placing it in the oven or blowing it with air before use. Then, the commercial SnO_2 nanoparticles (Quantum Solution Co.) were spin-coated onto a precleaned ITO glass substrate at 5000 rpm for 30 s, followed by a 30 min wait to dry the SnO_2 nanoparticle layer. The ink solution of $InBr_3$-capped InAs CQDs (concentration: 300 mg mL^{-1}) was dynamically spin-coated onto a SnO_2 layer-coated substrate at 3500 rpm for 40 s and 5000 rpm for 10 s in the glovebox. The fabrication of the InAs CQD photodetector was finalized by the sequential deposition of a 14 nm thick MoO_3 layer and a 140 nm thick Ag layer, which serves as the top contact electrode. The top Ag electrodes were deposited via thermal evaporation through a custom-built circular shadow mask, with varying pixel sizes, defining the effective active area (A) as the geometric overlap of the ITO bottom electrode and Ag top electrode.

Materials Characterization

Absorption Spectroscopy. The absorption spectrum was measured using a homemade setup consisting of QE Pro and NIR Quest spectrometers (Ocean Optics). The CQD solutions were put in a quartz cuvette with a path length of 1 mm. The cuvette was placed in a SQUARE ONE cuvette holder (Ocean Optics) connected to the spectrometers through optical fibers.

Photoluminescence (PL) Spectroscopy. The PL spectrum was obtained using a UV−vis spectrophotometer (HORIBA, Synapse and Symphony II). The solutions were loaded into a quartz cuvette with a 1 cm path length.

Transmission Electron Microscopy (TEM). Bright-field TEM and high-resolution TEM (HRTEM) images were acquired using a JEOL JEM-ARM300F GRAND ARM operating at an acceleration voltage of 300 kV. The CQD specimens were prepared by drop-casting diluted InAs CQD solutions onto carbon film-coated 300 mesh copper grids in an inert environment.

X-ray Diffractometry (XRD). The XRD data were collected using a powder X-ray diffractometer with Cu Kα radiation. The powder samples were prepared by drop-casting the InAs CQD solution onto the sample holder and then thoroughly drying them under vacuum.

Nuclear Magnetic Resonance (NMR). ^1H NMR spectra were recorded at room temperature using a 400 MHz Bruker Avance III HD Nanobay system, while ^2H NMR spectra were obtained using a 600 MHz Bruker Avance III system under the same conditions. All samples were dispersed in deuterated chloroform ($CDCl_3$).

Thermogravimetric Analysis (TGA). TGA measurements were performed using a TGA 5500 system to evaluate the thermal stability and composition of the samples. The measurements were conducted under a nitrogen (N_2) atmosphere to prevent oxidation or decomposition reactions that could occur due to atmospheric oxygen. The samples were heated at a controlled rate of 6 °C min^{-1}, ensuring precise thermal decomposition profiling.

Transient Absorption (TA) Spectroscopy. The femtosecond TA measurements were performed in a HARPIA commercial instrument (Light Conversion) equipped with Kymera 193i (Oxford Instruments) spectrometer and a broadband Si NMOS detector (Hamamatsu S3901 + C7884). An amplified 260 fs pulse train, centered at 1026 nm, with an average power of 20 W and a repetition rate of 50 kHz was generated from a Pharos Yb:KGW laser (Light Conversion). The pulse train was divided into three parts. An optical parametric amplifier (Orpheus, Light Conversion) was pumped with 17.5 W and generated a pulse train centered at 470 nm; this train served as the pump pulse and was further modulated at 40 Hz. For the probe pulse, 0.5 W of the initial 1026 nm pulse train was routed to a motorized delay stage, providing 7 ns of delay, and a white light supercontinuum was generated by attenuating it with a variable neutral density filter and focusing it into a YAG crystal. The remaining 2 W were not used in the experiment. The pump and probe beams were then focused onto the sample with a couple of parabolic mirrors to collect the transient signals. All experiments were performed at room temperature.

X-ray Absorption Spectroscopy. In K-edge X-ray absorption spectra (XAS) were captured at the Australian Synchrotron (ANSTO in Clayton, Victoria) XAS beamline 12-ID. A double-crystal Si (111) monochromator equipped with focusing optics was used to reduce harmonic content while producing excitation energy. The inline In metal foil (the initial peak of the first derivative occurs at 27938.7 eV) was used to calibrate the monochromator at In−K absorption edge with E_0 set to its reported value of 27939.9 eV.[37] All acquisitions were performed on powdered materials in a transmission mode. CQD powders were mixed with cellulose and pelletized as 7 mm diameter disks to mitigate absorption effects. Brief XAS scans of specific samples were conducted to verify the stability of the materials under at least several minutes of X-ray exposure before the full acquisitions.

https://doi.org/10.1021/jacs.6c03275
J. Am. Chem. Soc. XXXX, XXX, XXX−XXX

Samples were measured in a slew-scanning move with varying energy intervals over the pre-edge (5 eV) and the XANES region (0.25), with 0.035 intervals in k-space over the EXAFS. At low-k an integration time of 450 ms was employed per interval, with longer integration times weighted toward high-k portions of the spectrum, up to a maximum value of 18 in k-space (max of 1000 ms).

EXAFS Analysis. Multiple scans were collected at different positions of the sample. Data processing including background subtraction, scan averaging, edge-height normalization, and rebinning was performed based on the Athena program.[38] For normalization of energy spectra and removal of background, the pre-edge range was set between −170 and −50 eV, while the normalization range spanned from 150 to 1200 eV postedge. The order of normalization was designated as 3. For the presented EXAFS data, the k-weight was configured as 2 or 3, and the k-range for the forward Fourier transform was defined from 1.5 to 16. EXAFS fitting was conducted in the ARTEMIS, part of the IFEFFIT software package.[38] The scattering paths used to evaluate and model the data were derived from the optimized crystal structures of InAs and In_2O_3 considering their local structure/paths out to 3.5 Å. Using these input structures to derive the scattering paths, an agreeable fine structure accounting for the dominant EXAFS signal arising from an R fitting window of 1.5 to 3.8 Å emerged. The data were ultimately fit using 20 variables and 28 independent points, resulting in reasonable R-factors of less than 0.013 for all fits. The fitting was conducted in R-space using multiple k-weightings, with k = 1, 2, and 3. Errors of individual fit parameters were determined using ARTEMIS to take into account the correlations between parameters and known parameters without error estimates were fixed during the fit.

Device Performance Measurement

Current density versus voltage (J−V) characteristics at room temperature were measured using a Keithley 2450 source-measure unit (SMU). 1310 nm illumination was provided by a customized 4-channel fiber-coupled laser source (Thorlabs, MCLS1). The illumination density was determined using a calibrated S122C Germanium photodiode from Thorlabs. External quantum efficiency (EQE) was measured using an Oriel model QE-PV-SI instrument. Prior to measurement, the EQE system was calibrated with a NIST-certified silicon photodiode. The incident monochromatic light intensity used for the EQE measurement at 1520 nm was measured to be 0.651 mW/cm^2 using a Thorlabs PM100D optical power meter equipped with an S122C sensor. Responsivity (R) was calculated from EQE using $R = \mathrm{EQE} \times (\lambda q/hc)$, where q is the elementary charge, λ is the wavelength, h is Planck's constant, and c is the speed of light. Photocurrent transients were recorded with a Tektronix MS064B 8 GHz oscilloscope. A 260 fs pulse train centered at 1026 nm was generated by a Yb:KGW laser (Pharos, Light Conversion) operating at a repetition rate of 0.5 kHz. This pulse train was used to pump an optical parametric amplifier (Orpheus, Light Conversion), which was tuned to 1500 nm to illuminate the pixels. During optoelectronic characterization, a nonreflective mask with aperture sizes matching the shadow-mask-defined pixels was placed directly over the device to restrict illumination to the pixel and eliminate parasitic photocurrent from surrounding areas. The precise dimensions of the active areas were verified and provided by the mask vendor to ensure accurate calculation of current density and detectivity.

■ ASSOCIATED CONTENT

Supporting Information

The Supporting Information is available free of charge at https://pubs.acs.org/doi/10.1021/jacs.6c03275.

Time-dependent absorption spectra with excitonic peak evolution and peak-to-valley ratios for InAs CQD growth under varied long-chain carboxylic acid, nanocluster concentration, and injection rate conditions; schematic of monomer transport; partial and purification-dependent ^{1}H NMR with integration, TGA, transient absorption (TA), and DOSY data for acetic acid-functionalized nanoclusters; absorption/PL spectra of InAs nanoclusters and CQDs prepared with different short-chain carboxylic acids; In K-edge XANES/EXAFS analysis and fitting details; XRD patterns of the CQD series; acetic acid dose- and stage-dependent InAs CQD growth kinetics; SCLC analysis of oxide-free and surface-oxidized InAs CQD films; optical and structural characterization (absorption, FT-IR, and TEM) before and after ligand exchange; light intensity-dependent photocurrent response; and a benchmarking table of InAs CQD photodetector detectivity (PDF)

■ AUTHOR INFORMATION

Corresponding Author

Edward H. Sargent − *Department of Chemistry, Northwestern University, Evanston, Illinois 60208, United States; Department of Electrical and Computer Engineering, Northwestern University, Evanston, Illinois 60208, United States;* orcid.org/0000-0003-0396-6495; Email: ted.sargent@northwestern.edu

Authors

Hyeong Woo Ban − *Department of Chemistry, Northwestern University, Evanston, Illinois 60208, United States;* orcid.org/0000-0002-0691-2356

Xubiao Li − *Department of Chemistry, Northwestern University, Evanston, Illinois 60208, United States*

Stefan Zeiske − *Department of Chemistry, Northwestern University, Evanston, Illinois 60208, United States;* orcid.org/0000-0002-6598-3066

Julian A. Steele − *Australian Institute for Bioengineering and Nanotechnology & School of Mathematics and Physics, The University of Queensland, Brisbane, Queensland 4072, Australia*

Rafael Eduardo López-Arteaga − *Department of Chemistry, Northwestern University, Evanston, Illinois 60208, United States;* orcid.org/0000-0001-8058-3469

Haijiao Lu − *Nanomaterials Centre, School of Chemical Engineering & Australian Institute for Bioengineering and Nanotechnology, The University of Queensland, St Lucia, Queensland 4072, Australia;* orcid.org/0000-0001-9273-2898

Yalong Zou − *Nanomaterials Centre, School of Chemical Engineering & Australian Institute for Bioengineering and Nanotechnology, The University of Queensland, St Lucia, Queensland 4072, Australia*

Moon Gyu Han − *Samsung Advanced Institute of Technology, Samsung Electronics, Suwon 16678, Republic of Korea;* orcid.org/0000-0003-4223-3286

Tae-Gon Kim − *Samsung Advanced Institute of Technology, Samsung Electronics, Suwon 16678, Republic of Korea*

Cheng Liu − *Department of Chemistry, Northwestern University, Evanston, Illinois 60208, United States;* orcid.org/0000-0003-0258-4428

Bin Chen − *Department of Chemistry, Northwestern University, Evanston, Illinois 60208, United States;* orcid.org/0000-0002-2106-7664

Complete contact information is available at: https://pubs.acs.org/10.1021/jacs.6c03275

https://doi.org/10.1021/jacs.6c03275
J. Am. Chem. Soc. XXXX, XXX, XXX−XXX

Author Contributions

[▽]H.W.B. and X.L. contributed equally to this work.

Notes

The authors declare no competing financial interest.

■ ACKNOWLEDGMENTS

This work is supported by Samsung Advanced Institute of Technology, Samsung Electronics Co., Ltd. This work made use of the EPIC facility of Northwestern University's NUANCE Center, which has received support from the SHyNE Resource (NSF ECCS-2025633), the IIN (NIH-S10OD026871), and Northwestern's MRSEC program (NSF DMR-2308691). J.A.S. and H.L. acknowledge financial support from the Australian Research Council (DE230100173, DE230100357). Part of this work was conducted on the XAS beamline at the Australian Synchrotron, part of ANSTO.

■ REFERENCES

(1) Wang, Y.; Peng, L.; Schreier, J.; Bi, Y.; Black, A.; Malla, A.; Goossens, S.; Konstantatos, G. Silver telluride colloidal quantum dot infrared photodetectors and image sensors. *Nat. Photonics* **2024**, *18*, 236−242.

(2) Saran, R.; Curry, R. J. Lead sulphide nanocrystal photodetector technologies. *Nat. Photonics* **2016**, *10*, 81−92.

(3) Tang, X.; Ackerman, M. M.; Chen, M.; Guyot-Sionnest, P. Dual-band infrared imaging using stacked colloidal quantum dot photodiodes. *Nat. Photonics* **2019**, *13*, 277−282.

(4) Ding, F.; Zhan, Y.; Lu, X.; Sun, Y. Recent advances in near-infrared II fluorophores for multifunctional biomedical imaging. *Chem. Sci.* **2018**, *9*, 4370−4380.

(5) Erland, B. M.; Thorpe, A. K.; Gamon, J. A. Recent advances toward transparent methane emissions monitoring: A review. *Environ. Sci. Technol.* **2022**, *56*, 16567−16581.

(6) García de Arquer, F. P.; Talapin, D. V.; Klimov, V. I.; Arakawa, Y.; Bayer, M.; Sargent, E. H. Semiconductor quantum dots: Technological progress and future challenges. *Science* **2021**, *373*, No. eaaz8541.

(7) Talapin, D. V.; Lee, J.-S.; Kovalenko, M. V.; Shevchenko, E. V. Prospects of colloidal nanocrystals for electronic and optoelectronic applications. *Chem. Rev.* **2010**, *110*, 389−458.

(8) Konstantatos, G.; Howard, I.; Fischer, A.; Hoogland, S.; Clifford, J.; Klem, E.; Levina, L.; Sargent, E. H. Ultrasensitive solution-cast quantum dot photodetectors. *Nature* **2006**, *442*, 180−183.

(9) Houtepen, A. J.; Sargent, E. H.; Infante, I.; Owen, J. S.; Green, P. B.; Schaller, R. D.; Bals, S.; Zeiske, S.; Stöferle, T.; Hens, Z. Colloidal quantum dots for optoelectronics. *Nat. Rev. Methods Primers* **2025**, *5*, 42.

(10) Vafaie, M.; Fan, J. Z.; Morteza Najarian, A.; Ouellette, O.; Sagar, L. K.; Bertens, K.; Sun, B.; García de Arquer, F. P.; Sargent, E. H. Colloidal quantum dot photodetectors with 10-ns response time and 80% quantum efficiency at 1,550 nm. *Matter* **2021**, *4*, 1042−1053.

(11) Moreels, I.; Justo, Y.; De Geyter, B.; Haustraete, K.; Martins, J. C.; Hens, Z. Size-tunable, bright, and stable PbS quantum dots: A surface chemistry study. *ACS Nano* **2011**, *5*, 2004−2012.

(12) Clifford, J. P.; Konstantatos, G.; Johnston, K. W.; Hoogland, S.; Levina, L.; Sargent, E. H. Fast, sensitive and spectrally tuneable colloidal-quantum-dot photodetectors. *Nat. Nanotechnol.* **2009**, *4*, 40−44.

(13) Keuleyan, S. E.; Guyot-Sionnest, P.; Delerue, C.; Allan, G. Mercury telluride colloidal quantum dots: Electronic structure, size-dependent spectra, and photocurrent detection up to 12 μm. *ACS Nano* **2014**, *8*, 8676−8682.

(14) Lhuillier, E.; Keuleyan, S.; Liu, H.; Guyot-Sionnest, P. Mid-IR colloidal nanocrystals. *Chem. Mater.* **2013**, *25*, 1272−1282.

(15) Choi, M.-J.; Sagar, L. K.; Sun, B.; Biondi, M.; Lee, S.; Najjariyan, A. M.; Levina, L.; García de Arquer, F. P.; Sargent, E. H. Ligand exchange at a covalent surface enables balanced stoichiometry in III-V colloidal quantum dots. *Nano Lett.* **2021**, *21*, 6057−6063.

(16) Sun, B.; Najarian, A. M.; Sagar, L. K.; Biondi, M.; Choi, M. J.; Li, X.; Levina, L.; Baek, S. W.; Zheng, C.; Lee, S.; et al. Fast near-infrared photodetection using III-V colloidal quantum dots. *Adv. Mater.* **2022**, *34*, 2203039.

(17) Srivastava, V.; Dunietz, E.; Kamysbayev, V.; Anderson, J. S.; Talapin, D. V. Monodisperse InAs quantum dots from aminoarsine precursors: Understanding the role of reducing agent. *Chem. Mater.* **2018**, *30*, 3623−3627.

(18) Asor, L.; Liu, J.; Ossia, Y.; Tripathi, D. C.; Tessler, N.; Frenkel, A. I.; Banin, U. InAs Nanocrystals with Robust p-Type Doping. *Adv. Funct. Mater.* **2021**, *31*, 2007456.

(19) Grigel, V.; Dupont, D.; De Nolf, K.; Hens, Z.; Tessier, M. D. InAs colloidal quantum dots synthesis via aminopnictogen precursor chemistry. *J. Am. Chem. Soc.* **2016**, *138*, 13485−13488.

(20) Ban, H. W.; Vafaie, M.; Levina, L.; Xia, P.; Imran, M.; Liu, Y.; Najarian, A. M.; Sargent, E. H. Resurfacing of InAs colloidal quantum dots equalizes photodetector performance across synthetic routes. *J. Am. Chem. Soc.* **2024**, *146*, 24935−24944.

(21) Franke, D.; Harris, D. K.; Chen, O.; Bruns, O. T.; Carr, J. A.; Wilson, M. W. B.; Bawendi, M. G. Continuous injection synthesis of indium arsenide quantum dots emissive in the short-wavelength infrared. *Nat. Commun.* **2016**, *7*, 12749.

(22) Ginterseder, M.; Franke, D.; Perkinson, C. F.; Wang, L.; Hansen, E. C.; Bawendi, M. G. Scalable synthesis of InAs quantum dots mediated through indium redox chemistry. *J. Am. Chem. Soc.* **2020**, *142*, 4088−4092.

(23) Tamang, S.; Lee, S.; Choi, H.; Jeong, S. Tuning size and size distribution of colloidal InAs nanocrystals via continuous supply of prenucleation clusters on nanocrystal seeds. *Chem. Mater.* **2016**, *28*, 8119−8122.

(24) Song, J. H.; Choi, H.; Pham, H. T.; Jeong, S. Energy level tuned indium arsenide colloidal quantum dot films for efficient photovoltaics. *Nat. Commun.* **2018**, *9*, 4267.

(25) Shin, J.; Choi, M.; Shim, D.; Ziehl, T. J.; Park, S.; Cho, E.; Zhang, P.; Lee, H.; Kang, J.; Jeong, S. Unveiling the nanocluster conversion pathway for highly monodisperse InAs colloidal quantum dots. *JACS Au* **2024**, *4*, 1097−1106.

(26) Kim, T.; Park, S.; Jeong, S. Diffusion dynamics controlled colloidal synthesis of highly monodisperse InAs nanocrystals. *Nat. Commun.* **2021**, *12*, 3013.

(27) Kim, M.; Lee, J.; Jung, J.; Shin, D.; Kim, J.-W.; Cho, E.; Xing, Y.; Jeong, H.; Park, S.; Park, T. G.; et al. Surface-originated weak confinement in tetrahedral indium arsenide quantum dots. *J. Am. Chem. Soc.* **2024**, *146*, 10251−10256.

(28) Skorotetcky, M. S.; Mir, S. H.; Sheikh, T.; Yorov, K. E.; Saidzhonov, B.; Daws, A. A.; Zhou, C.; Hedhili, M. N.; Abulikemu, M.; Mohammed, O. F.; et al. Si-H hydrosilane reducing agents for size- and shape-controlled InAs colloidal quantum dots. *Adv. Mater.* **2025**, *37*, No. 2412105.

(29) Vafaie, M.; Morteza Najarian, A.; Xu, Y.; Richter, A. F.; Li, J.; Zhang, D.; Imran, M.; Xia, G.; Ban, H. W.; Levina, L.; et al. Molecular surface programming of rectifying junctions between InAs colloidal quantum dot solids. *Proc. Natl. Acad. Sci. U.S.A.* **2023**, *120*, No. e2305327120.

(30) Fritzinger, B.; Capek, R. K.; Lambert, K.; Martins, J. C.; Hens, Z. Utilizing self-exchange to address the binding of carboxylic acid ligands to CdSe quantum dots. *J. Am. Chem. Soc.* **2010**, *132*, 10195−10201.

(31) De Nolf, K.; Capek, R. K.; Abe, S.; Sluydts, M.; Jang, Y. J.; Martins, J. C.; Cottenier, S.; Lifshitz, E.; Hens, Z. Controlling the size of hot injection made nanocrystals by manipulating the diffusion coefficient of the solute. *J. Am. Chem. Soc.* **2015**, *137*, 2495−2505.

(32) Tamang, S.; Lincheneau, C.; Hermans, Y.; Jeong, S.; Reiss, P. Chemistry of InP nanocrystal syntheses. *Chem. Mater.* **2016**, *28*, 2491−2506.

https://doi.org/10.1021/jacs.6c03275
J. Am. Chem. Soc. XXXX, XXX, XXX−XXX

(33) Almeida, G.; Ubbink, R. F.; Stam, M.; du Fossé, I.; Houtepen, A. J. InP colloidal quantum dots for visible and near-infrared photonics. *Nat. Rev. Mater.* **2023**, *8*, 742−758.
(34) De Nolf, K.; Cosseddu, S. M.; Jasieniak, J. J.; Drijvers, E.; Martins, J. C.; Infante, I.; Hens, Z. Binding and Packing in Two-Component Colloidal Quantum Dot Ligand Shells: Linear versus Branched Carboxylates. *J. Am. Chem. Soc.* **2017**, *139*, 3456−3464.
(35) Leemans, J.; Pejovic, V.; Georgitzikis, E.; Minjauw, M.; Siddik, A. B.; Deng, Y.-H.; Kuang, Y.; Roelkens, G.; Detavernier, C.; Lieberman, I.; Malinowski, P. E.; Cheyns, D.; Hens, Z. Colloidal III-V quantum dot photodiodes for short-wave infrared photodetection. *Adv. Sci.* **2022**, *9*, No. 2200844.
(36) Shin, D.; Jeong, H.; Kim, J.; Jang, E.; Park, Y.; Jeong, S. High performance infrared InAs colloidal quantum dot photodetector with 79% EQE enabled by an extended absorber layer. *Adv. Opt. Mater.* **2025**, *13*, 2401931.
(37) Kraft, S.; Stümpel, J.; Becker, P.; Kuetgens, U. High resolution x-ray absorption spectroscopy with absolute energy calibration for the determination of absorption edge energies. *Rev. Sci. Instrum.* **1996**, *67*, 681−687.
(38) Ravel, B.; Newville, M. ATHENA, ARTEMIS, HEPHAESTUS: Data analysis for x-ray absorption spectroscopy using IFEFFIT. *J. Synchrotron Radiat.* **2005**, *12*, 537−541.

https://doi.org/10.1021/jacs.6c03275
J. Am. Chem. Soc. XXXX, XXX, XXX−XXX